lubricants

MDPI

Article

Optimization of Preparation Process Parameters for HVOF-Sprayed WC-10Co-4Cr Coatings and Study of Abrasive and Corrosion Performances

Tao Liu [1], Jiajun Li [2], Haifeng Li [3], Jianwu Liu [3], Yueyu Huang [2], Qun Wang [2,*] and Chidambaram Seshadri Ramachandran [4]

[1] Petroleum Engineering and Technology Institute of Southwest Oil and Gas Branch, Sinopec, Deyang 618000, China; liutao.xnyq@sinopec.com
[2] College of Materials Science and Engineering, Hunan University, Changsha 410082, China; 15673299868@163.com (J.L.); 17758586244@163.com (Y.H.)
[3] Transmission R&D Center, AECC Hunan Aviation Powerplant Research Institute, Zhuzhou 412002, China; lihaifeng3737@163.com (H.L.); jianwuliu8678@163.com (J.L.)
[4] Department of Materials Science and Engineering, State University of New York at Stony Brook, New York, NY 11794, USA; csrcn1@gmail.com
* Correspondence: wangqun@hun.edu.cn

Abstract

To enhance the abrasive wear resistance of mechanical components operating in corrosive environments, this study fabricated WC-10Co-4Cr coatings using high-velocity oxygen-fuel (HVOF) thermal spraying technology. A L9 (3^4) orthogonal array was designed to optimize four key process parameters (kerosene flow rate, oxygen flow rate, powder feed rate, and spraying distance) at three levels each, aiming for minimal porosity. The phase composition, microstructure, hardness, abrasive wear resistance, and corrosion resistance of the coatings were systematically characterized by X-ray diffraction (XRD), scanning electron microscopy (SEM) with energy dispersive spectroscopy (EDS), microhardness tester, wet sand rubber wheel abrasion tester, and electrochemical workstation. The results indicated that the optimal parameters were a kerosene flow rate of 0.0073 L/s, oxygen flow rate of 15.33 L/s, powder feed rate of 1 g/s, and spraying distance of 326 mm. The coating prepared under these conditions exhibited high density with a porosity of only 0.32% and a high microhardness of 1281 HV1. Compared to the AISI 1020 steel substrate, the optimized WC-10Co-4Cr coating demonstrated a 122-fold improvement in abrasive wear resistance and a better corrosion resistance, showcasing its excellent overall performance and great potential for wear-resistant surface protection in corrosive environments.

Keywords: HVOF; WC-10Co-4Cr coating; process optimization; abrasive wear; corrosion resistance

check for updates

Received: 30 September 2025
Revised: 25 November 2025
Accepted: 26 November 2025
Published: 27 November 2025

Citation: Liu, T.; Li, J.; Li, H.; Liu, J.; Huang, Y.; Wang, Q.; Ramachandran, C.S. Optimization of Preparation Process Parameters for HVOF-Sprayed WC-10Co-4Cr Coatings and Study of Abrasive and Corrosion Performances. *Lubricants* **2025**, *13*, 516. https://doi.org/10.3390/lubricants13120516

Copyright: © 2025 by the authors. Licensee MDPI, Basel, Switzerland. This article is an open access article distributed under the terms and conditions of the Creative Commons Attribution (CC BY) license (https://creativecommons.org/licenses/by/4.0/).

1. Introduction

WC-CoCr cermet coatings are widely applied for surface protection of key components in hydraulic machinery, marine equipment, and the petrochemical industry due to their exceptional hardness, excellent wear resistance, and good corrosion resistance, which help resist abrasive wear and corrosion under harsh service conditions [1–3]. High-Velocity Oxygen-Fuel (HVOF) thermal spraying technology is considered one of the most effective methods for preparing WC-based coatings [4,5]. Its relatively low flame temperature and high particle velocity effectively inhibit decarburization and decomposition of WC particles

during flight, resulting in coatings with dense structures, high bond strength, and superior wear and corrosion resistance [6].

However, the HVOF spraying process is complex, involving multi-physical field coupling, and the coating properties are highly dependent on process parameters such as fuel flow rate, oxygen flow rate, powder feed rate, and spraying distance [7]. Inappropriate parameter combinations can lead to high porosity, unmelted particles, excessive oxidation, or even severe decarburization of WC, forming brittle phases like W_2C and η-phase (e.g., Co_3W_3C, Co_6W_6C), significantly degrading the mechanical properties and service life of the coating [4,6,8]. Therefore, systematic optimization of HVOF spray parameters is crucial for obtaining coatings with optimal performance.

Numerous studies have been conducted on HVOF- or HVAF-sprayed WC-CoCr coatings. For instance, Wang et al. comparatively analyzed the wear and corrosion performance of WC-10Co-4Cr coatings deposited by different HVOF and HVAF spraying processes and demonstrated that HVAF coatings possess denser structures and improved corrosion resistance compared to HVOF ones [9]. Further, Wang et al. reported that both WC- and Cr_3C_2-based coatings produced by HVOF exhibit excellent wear, erosion, and corrosion resistance, indicating their potential to replace electrolytic hard chrome coatings [10]. The effect of binder composition was also clarified by Wang et al., who showed that the variation in Co and Cr content significantly affects the microstructure, hardness, and corrosion resistance of WC-Co-Cr coatings [11]. In addition, Xing et al. and Singh et al. investigated the corrosion performance of WC-CoCr coatings applied to offshore hydraulic components and boiler steels, respectively, highlighting the importance of interface density and phase stability in corrosion protection [12,13].

While these studies enrich the understanding of coating properties, most concentrate on performance characterization under fixed parameters or simple adjustments of single parameters. Previous research in this field has not provided an in-depth discussion on pore formation and corrosion mechanisms in HVOF sprayed WC-based coatings. This paper classifies the shapes and types of pores in the cross-section of WC-based coatings, as well as typical characteristics in the surface morphology after corrosion, and conducts further thorough analysis and discussion based on this classification. The study enhances readers' understanding of performance regulation in HVOF-sprayed WC-based coatings, which precisely reflects the novelty and originality of this paper. Furthermore, research employing scientific Design of Experiments (DOE) methods, such as orthogonal arrays, to systematically optimize multiple key process parameters and simultaneously investigate their effects on microstructure and comprehensive performance, especially the synergy between abrasive wear and corrosion resistance, remains insufficient [8,12–14].

Therefore, this study aims to optimize four key process parameters (kerosene flow rate, oxygen flow rate, powder feed rate, and spraying distance) for HVOF-sprayed WC-10Co-4Cr coatings using an orthogonal experimental design, with coating porosity as the primary optimization target. Based on this, the phase composition, microstructure, and microhardness of the coating under the optimal process were systematically analyzed. Particular focus was placed on investigating its wear mechanism under wet abrasive wear conditions and its electrochemical corrosion behavior. The goal is to provide theoretical and experimental basis for preparing high-performance WC-CoCr coatings suitable for severe corrosive-wear conditions.

2. Experimental Materials and Methods

2.1. Coating Preparation and Experimental Design

The spray powder was commercial agglomerated and sintered WC-10Co-4Cr powder (particle size range: 10–38 μm). The powder morphologies are shown in Figure 1.

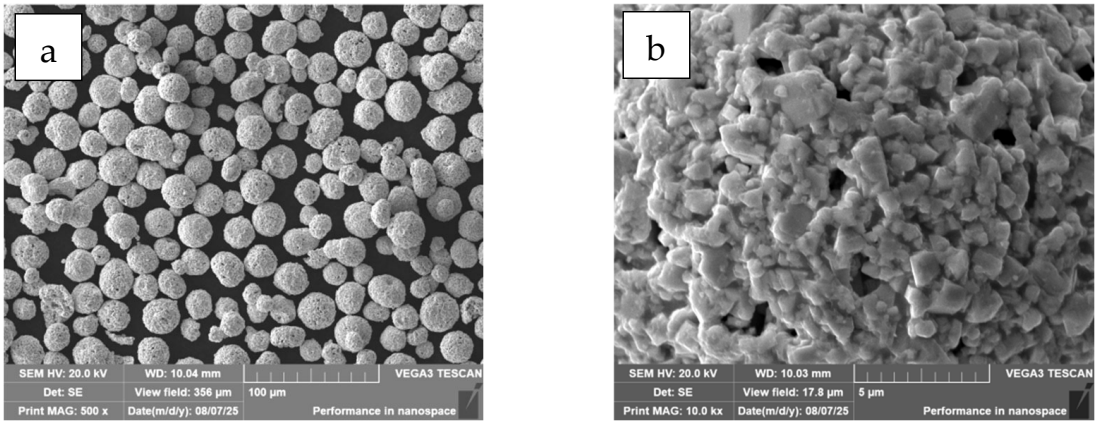


Figure 1. Morphologies of the WC-10Co-4Cr powder: (**a**) low magnification, (**b**) high magnification of a single powder particle.

As shown in Figure 1a, all WC-10Co-4Cr powders exhibit a near-spherical morphology. Each individual sphere is formed by the agglomeration of WC particles with a grain size of approximately 0.8 µm and an alloy binding phase, with some pores present on the surface of the powder particles (Figure 1b). This powder, with its moderate apparent density (5.1 g/cm^3), not only possesses high powder strength but also facilitates uniform heating in HVOF spraying, leading to the softening and melting of the binding phase. Consequently, a high-performance coating is achieved.

WC-10Co-4Cr coatings were prepared using a Praxair JP-8000 HVOF system (Linde Surface Technologies, Danbury, CT, USA). An L9 (3^4) orthogonal array was used, with four factors and three levels each, based on engineering experience and typical equipment parameter ranges: kerosene flow rate (Factor A: 0.0063, 0.0068, 0.0073 L/s), oxygen flow rate (Factor B: 14.13, 15.33, 16.53 L/s), powder feed rate (Factor C: 1, 1.25, 1.5 g/s), and spraying distance (Factor D: 326, 353, 380 mm). The other parameters were kept constant, for example: the powder feed gas flow was 0.167 L/s, the gun traverse speed was 500 mm/s, and the step size was 5 mm. Prior to the spraying process, rectangular AISI 1020 steel samples (Chemical composition in weight percent: C: 0.18–0.23, Mn: 0.30–0.60, P: $\leq$0.040, S: $\leq$0.050, and balance Fe) with dimensions of 100 × 60 × 6 mm^3 and a Vickers hardness of HV160 were subjected to degreasing, followed by grit blasting with 60-mesh alumina. The substrates were then preheated to approximately 100 °C using the spraying flame stream. In addition, the surface roughness was Ra 2.92–3.41 µm for the sandblasted substrate and Ra 3.23–4.14 µm for the as-sprayed coating and their three-dimensional surface morphologies were shown in Figure 2.

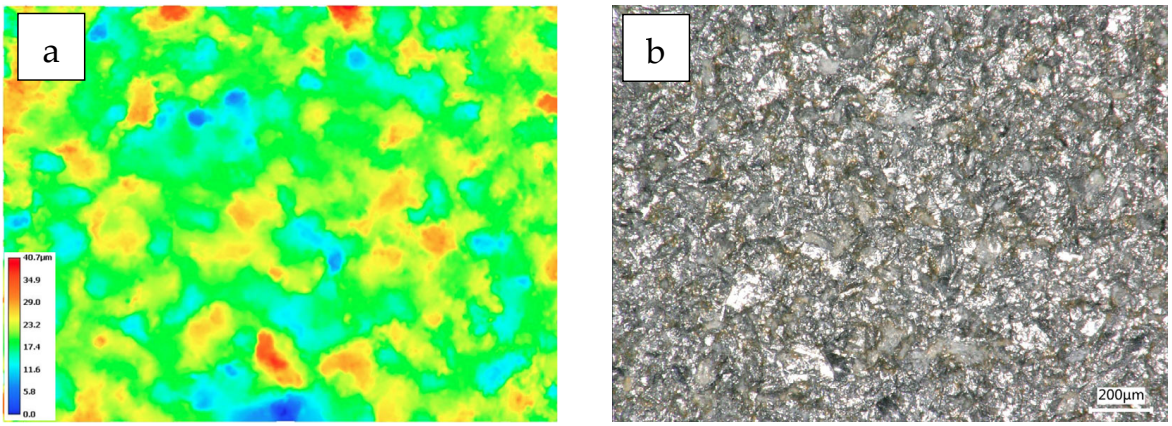


Figure 2. *Cont.*

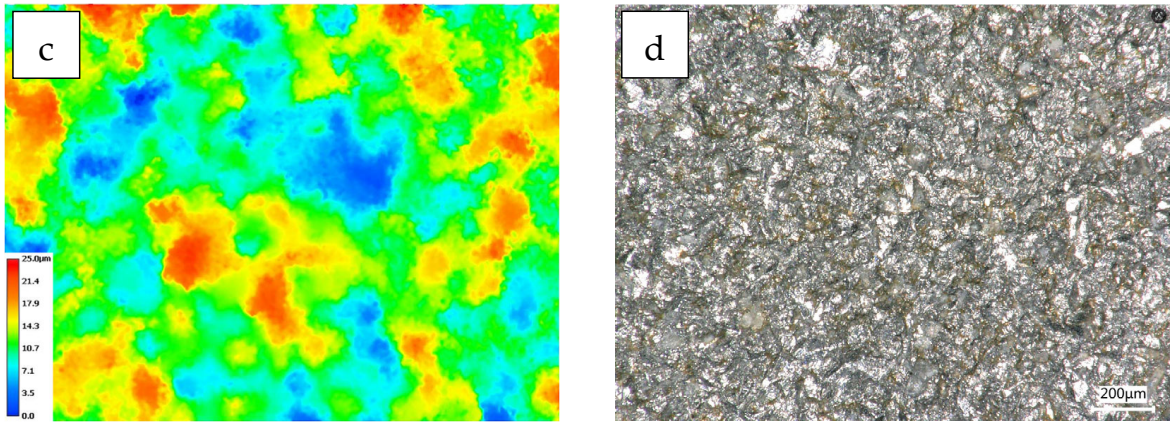


Figure 2. The three-dimensional surface morphologies: (**a**,**b**) the AISI 1020 steel substrate after grit blasting, (**c**,**d**) HVOF sprayed WC-10Co-4Cr coating.

2.2. Coating Characterization

2.2.1. Phase Composition Analysis

The phase composition of the spray powder and coatings was analyzed using a D/max-2550 X-ray diffractometer (Rigaku, Tokyo, Japan) with Cu Kα radiation, scanning range 30–90°, scan speed 5°/min, step size 0.02°.

2.2.2. Morphology and Microstructure Observation

The morphology of the original powder and the surface/cross-sectional morphology of the coatings, as well as worn and corroded surfaces, were observed using a MIRA3 LMH scanning electron microscope (TESCAN, Brno, Czech Republic) equipped with an Oxford One Max 20 EDS detector.

Micro-area composition analysis was performed using an energy-dispersive X-ray spectroscopy (EDS) system (Oxford Instruments, Abingdon, UK). Coating porosity was statistically calculated from cross-sectional SEM images using Image-Pro Plus software (version 7.0), averaging values from 10 different fields of view.

2.2.3. Bond Strength Tests

The bond strength of the WC-10Co-4Cr coating on the AISI 1020 steel substrate was evaluated in accordance with the ASTM C633-13 [15]. A cylindrical AISI 1020 steel specimen (ϕ25.4 mm × 50 mm) coated on one end was adhesively bonded to an uncoated counterpart of identical dimensions using a high-strength epoxy adhesive. The assembly was then mounted in the testing machine, and a uniaxial tensile load was applied at a loading rate of 0.0167 mm/s until failure occurred. The bond strength—representing either the adhesion between the coating and substrate or the cohesion within the coating—was calculated by dividing the maximum tensile load by the cross-sectional area of the specimen end face.

2.2.4. Microhardness Test

The cross-sectional microhardness of the coatings was measured using a HX-1000 microhardness tester (Shanghai Taiming Optical Instrument Co., Ltd., Shanghai, China) with a load of 1 kgf (9.81 N) and a dwell time of 15 s. At least 10 random points were measured per sample, and the average value was taken.

2.2.5. Abrasive Wear Test

The coated specimens, with dimensions of 57 × 25 × 6.3 mm^3, were tested using a MLS-225 wet sand rubber wheel abrasion tester (Zhangjiakou Chengxin Testing Equipment Manufacturing Co., Ltd., Zhangjiakou, China), in accordance with ASTM G105-20 [16].

Quartz sand with a grit size of 40–70 mesh was used as the abrasive medium. The applied load was 100 N, the rubber wheel speed was 240 rpm (4 r/s), and the total number of revolutions was 3000.

The wear rate was calculated based on the weight loss (accuracy ± 0.1 mg) and compared with that of the AISI 1020 steel substrate. The worn surface morphologies were examined using SEM to analyze the wear mechanisms and dominant abrasion features.

2.2.6. Electrochemical Corrosion Test

Electrochemical corrosion tests were conducted using a CHI660E electrochemical workstation (Shanghai CH Instruments, Inc., Shanghai, China) in a 3.5 wt.% NaCl solution. A conventional three-electrode system was employed, with the coating sample as the working electrode (exposed area 1 cm^2), a platinum electrode as the counter electrode, and a saturated calomel electrode (SCE) as the reference electrode. The sample was stabilized at the open-circuit potential (OCP) for 30 min prior to testing. Potentiodynamic polarization curves were scanned from −1.0 V to +0.5 V (vs. OCP) at a scan rate of 1 mV/s.

The corrosion potential (E_{corr}) and corrosion current density (I_{corr}) were determined by Tafel extrapolation, in accordance with ASTM G59-97 [17] and ASTM G102-89 [18], using the linear portions of the anodic and cathodic branches of the polarization curve [13]. The intersection point of these extrapolated lines was defined as E_{corr} and I_{corr} [8].

3. Results and Discussion

3.1. Phase Composition

The XRD patterns of the WC-10Co-4Cr spray powder and the nine corresponding coatings are shown in Figure 3.

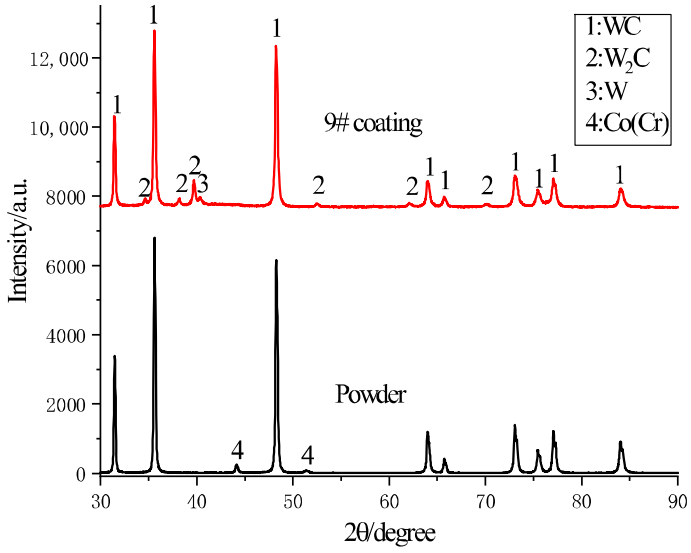


Figure 3. XRD patterns of the WC-10Co-4Cr powder and the corresponding coatings.

The phase composition of the nine coatings was essentially identical. The main phase in all coatings, as in the powder, was WC. However, the original CoCr phase present in the powder disappeared, replaced by small amounts of W_2C phase and trace amounts of W phase. This indicates that only very slight oxidation and decarburization of WC occurred during HVOF spraying [6]. Compared to plasma spraying [4,19], the flame temperature of kerosene-fueled HVOF [2,3] is much lower (around 1800 °C), while the particle velocity is nearly twice that of plasma spraying. This results in particles experiencing lower temperatures for a shorter time, leading to minimal decarburization of WC.

3.2. Cross-Sectional Microstructure

The cross-sectional morphologies of the coatings with the highest (3# coating) and lowest (9# coating) porosity are shown in Figure 4.

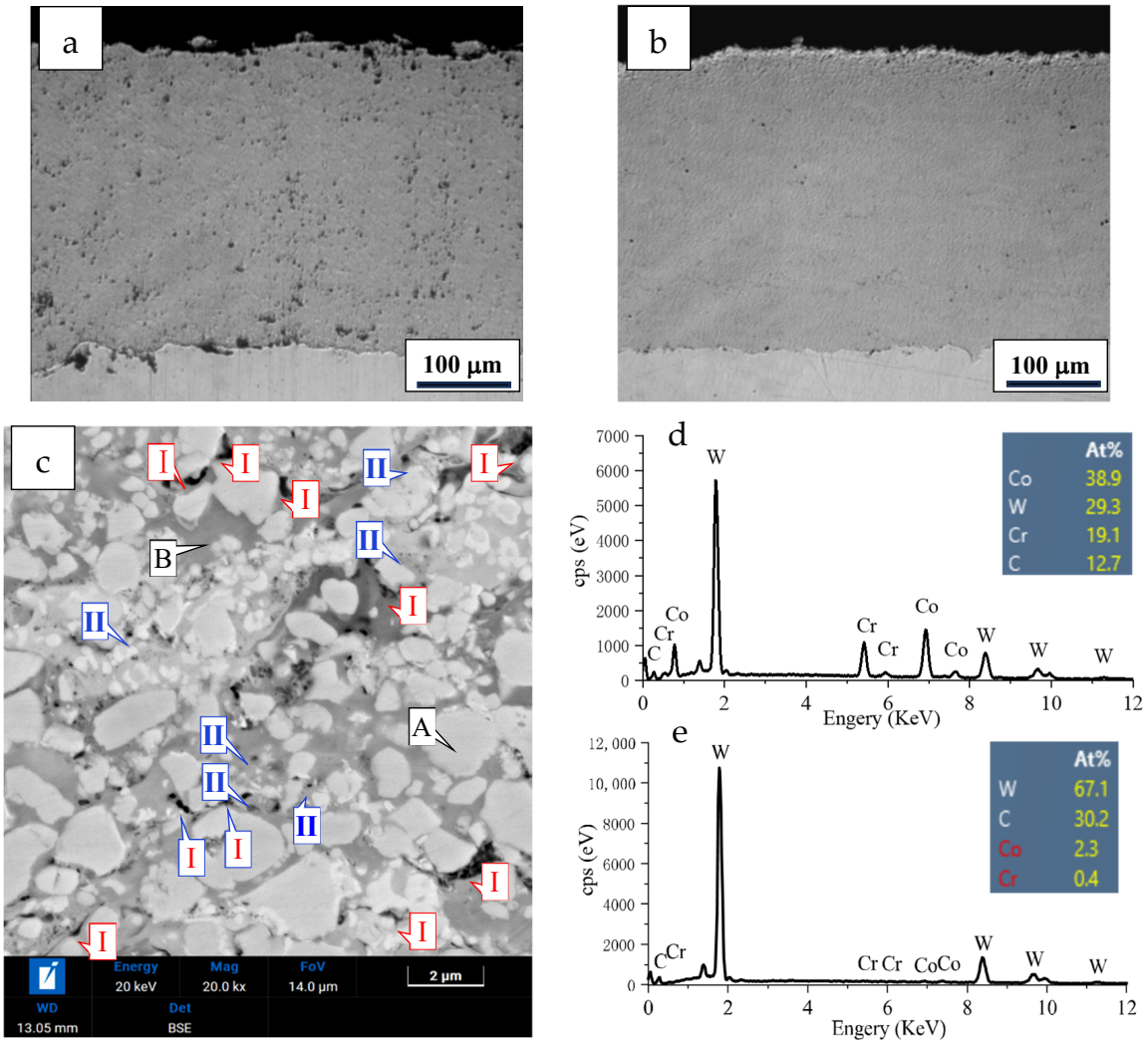


Figure 4. Cross-sectional morphology and EDS of coatings: (**a**) low-magnification OM image of sample 3#; (**b**) low-magnification OM image of sample 9#; (**c**) high-magnification BSE image of sample 9#; (**d**) EDS at position A; (**e**) EDS at position B. (I—small round pores; II—larger irregular pores; A—WC; B—CoCr binder).

Figure 4 shows that the porosity of coatings sprayed with the same powder but different HVOF parameters varied significantly [5,20]. 3# coating had the highest porosity (1.55%), while 9# coating had the lowest porosity (0.32%), indicating a strong influence of spray parameters. The coating under these conditions exhibited the highest hardness (1281 HV1) and the lowest porosity (0.32%). Increasing kerosene and oxygen flows raises the combustion enthalpy and in-flight gas momentum, which increases particle temperature and velocity so particles are more fully melted and impact the substrate with higher kinetic energy to form flatter, well-bonded splats and a denser coating; conversely, reducing powder feed rate gives each particle more residence time in the hot jet (fewer cold or partially melted particles per unit time), and shortening spray distance reduces in-flight cooling and deceleration—together these effects reduce unmelted cores, inter-splat voids and oxidation, producing the higher hardness and lower porosity observed for 9# coating [2,4,9]. In addition, during the bond strength test of 9# coating, fracture occurred at the adhesive

interface rather than at the coating-substrate interface, indicating that the actual bond strength between the coating and the substrate was not lower than the measured value of 75.6 MPa. However, even the highly dense 9# coating contained micropores (Figure 4c), which existed in two main forms: (1) Type I pores: Larger, irregularly shaped (e.g., elongated, triangular) pores (marked I in Figure 4c) primarily formed due to incomplete melting and/or insufficient deformation of the spray particles upon impact, resulting in inadequate filling of interstices between partially melted carbide particles and the binder phase [2,6,9]. This is often associated with non-optimal in-flight particle characteristics (temperature and velocity) [2,4] and inappropriate powder morphology or spray parameters [6,7,20]. (2) Type II pores: Smaller, rounded pores within the binder phase or at carbide/binder interfaces, caused by gas entrapment during melting/flight/deposition or gases (CO_2/CO) from WC oxidation/decarburization being trapped in the molten binder and not escaping before solidification (marked II in Figure 4c). Therefore, using WC powder with a homogeneous binder distribution is essential (reducing Type I pores), and optimizing HVOF parameters is crucial to ensure high particle velocity (promoting sufficient deformation, reducing Type I pores) without overheating (minimizing WC decarburization, reducing Type II pores).

3.3. Influence of HVOF Parameters on Coating Hardness

The microhardness and porosity results for the nine coatings from the orthogonal experiment are listed in Table 1.

Table 1. Coating hardness and porosity results of the orthogonal experiment.

Coating No.	Kerosene Flux (L/s)	Oxygen Flux (L/s)	Feed Rate (g/s)	Spraying Distance (mm)	Hardness (HV1)	Porosity (%)
1#	0.0063(A1)	14.13(B1)	1(C1)	326(D1)	1148 ± 110	1.12 ± 0.11
2#	0.0063(A1)	15.33(B2)	1.25(C2)	353(D2)	1098 ± 111	1.21 ± 0.17
3#	0.0063(A1)	16.53(B3)	1.5(C3)	380(D3)	1061 ± 98	1.55 ± 0.21
4#	0.0068(A2)	14.13(B1)	1.25(C2)	380(D3)	1139 ± 83	1.09 ± 0.18
5#	0.0068(A2)	15.33(B2)	1.5(C3)	326(D1)	1219 ± 78	0.79 ± 0.13
6#	0.0068(A2)	16.53(B3)	1(C1)	353(D2)	1187 ± 109	0.61 ± 0.09
7#	0.0073(A3)	14.13(B1)	1.5(C3)	353(D2)	1148 ± 86	0.81 ± 0.09
8#	0.0073(A3)	15.33(B2)	1(C1)	380(D3)	1205 ± 109	0.51 ± 0.05
9#	0.0073(A3)	16.53(B3)	1.25(C2)	326(D1)	1281 ± 72	0.32 ± 0.04
k1 (hardness)	1102.3	1145.0	1180.0	1216.0		
k2 (hardness)	1181.7	1174.0	1172.7	1144.3		
k3 (hardness)	1211.3	1176.3	1142.7	1135.0		
Range (hardness)	109.0	31.3	37.3	81.0		
Order of Influence	A > D > C > B					
Optimal Level and Combination (hardness)	0.0073(A3)	16.53(B3)	1(C1)	326(D1)		
k1 (porosity)	1.29	1.01	0.75	0.74		
k2 (porosity)	0.83	0.84	0.87	0.88		
k3 (porosity)	0.55	0.83	1.05	1.05		
Order of Influence	0.75	0.18	0.30	0.31		
Optimal Level and Combination (porosity)	0.0073(A3)	16.53(B3)	1(C1)	326(D1)		

To clarify the effects of individual parameters on coating hardness and porosity, a second-order polynomial regression was applied using the orthogonal experimental data (Table 1). The regression equations were established as follows (1) and (2):

$$\text{Hardness (HV1)} = 1138.2 + 540.6A + 22.4B - 18.3C - 45.1D - 112.7A^2 - 9.8B^2 - 6.4C^2 + 8.2D^2 \quad (1)$$

$$\text{Porosity (\%)} = 1.04 - 0.0063A - 0.07B + 0.04C + 0.05D + 0.11A^2 + 0.02B^2 + 0.03C^2 - 0.02D^2 \quad (2)$$

The regression coefficients indicate that kerosene flux (A) has the most significant positive influence on hardness and a strong negative effect on porosity, followed by spraying distance (D). The fitted curves show that hardness increases with higher kerosene flux and moderate oxygen flow, while porosity decreases markedly under the same conditions. The R^2 values of 0.94 (hardness) and 0.91 (porosity) demonstrate excellent fitting accuracy, confirming that the quadratic polynomial model effectively captures the nonlinear relationships among spraying parameters and coating properties.

The regression graphs showing the relationship between the hardness and porosity of the WC-10Co-4Cr coatings and the four factors of HVOF spraying are presented in Figures 5 and 6, respectively.

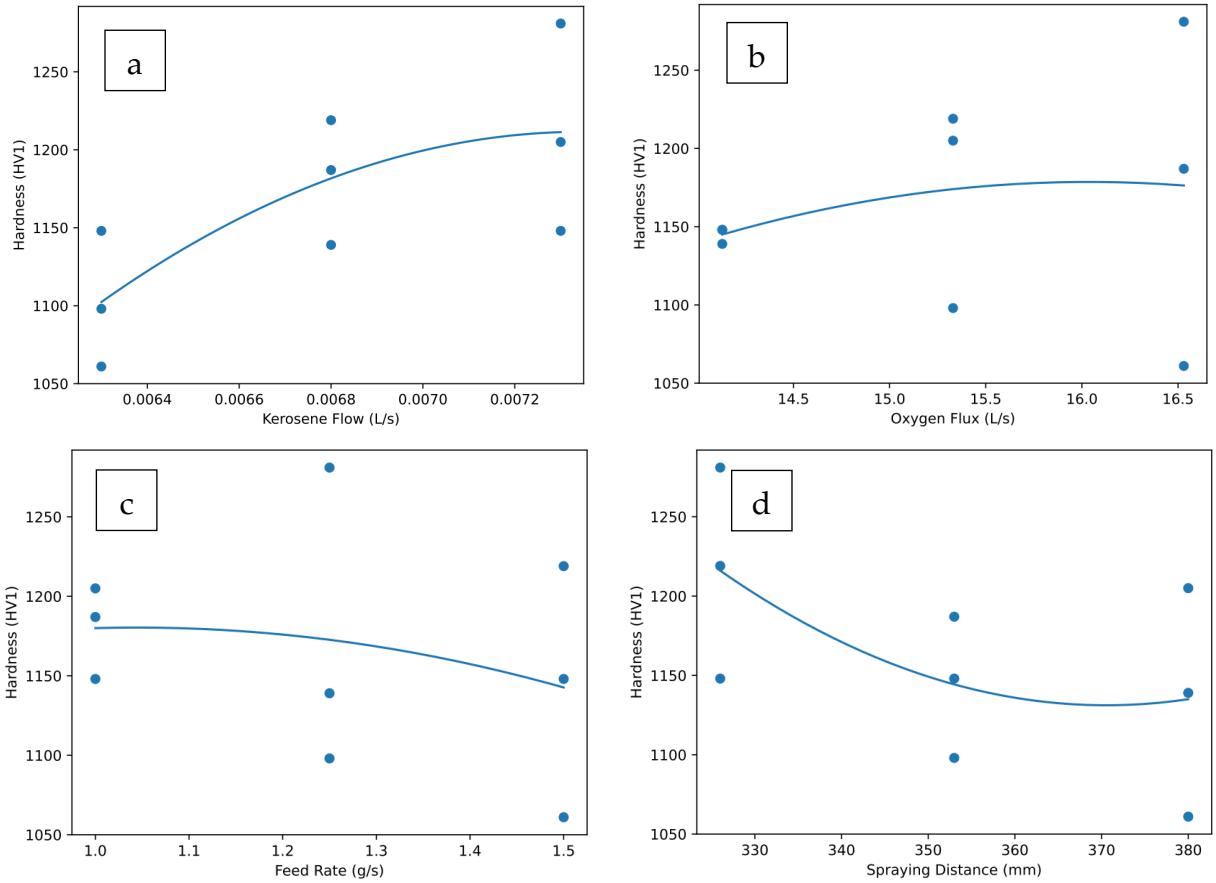


Figure 5. The regression graphs showing the relationship between the hardness of the WC-10Co-4Cr coating and the four factors of high-velocity oxygen-fuel (HVOF) spraying: (**a**) kerosene flow, (**b**) oxygen flow, (**c**) feed rate, (**d**) spray distance.

Combining Table 1 and Figures 5 and 6, it is evident that kerosene flow rate and spraying distance have the most significant influence on coating hardness and porosity. Adjusting these parameters is the most direct and effective way to change hardness and porosity. Spraying distance also has a noticeable effect, while oxygen flow rate has the least influence. As presented in Table 1, the "Range" of a factor is defined as the difference between its highest and lowest mean values (k1, k2, k3). These k-values correspond to the average outcomes (e.g., hardness, porosity) observed when the factor is set to level 1, 2, or 3. A larger range indicates that the factor has a greater influence on the response. The

order of influence of spraying parameters on coating hardness and porosity is as follows: kerosene flow rate > spraying distance > powder feed rate > oxygen flow rate. With the exception of oxygen flow rate, the optimal parameters for achieving the highest hardness and the lowest porosity are identical; therefore, the optimal spraying parameters are set as follows: kerosene flow rate (0.0073 L/s), spraying distance (326 mm), powder feed rate (1 g/s), and oxygen flow rate (15.33 L/s).

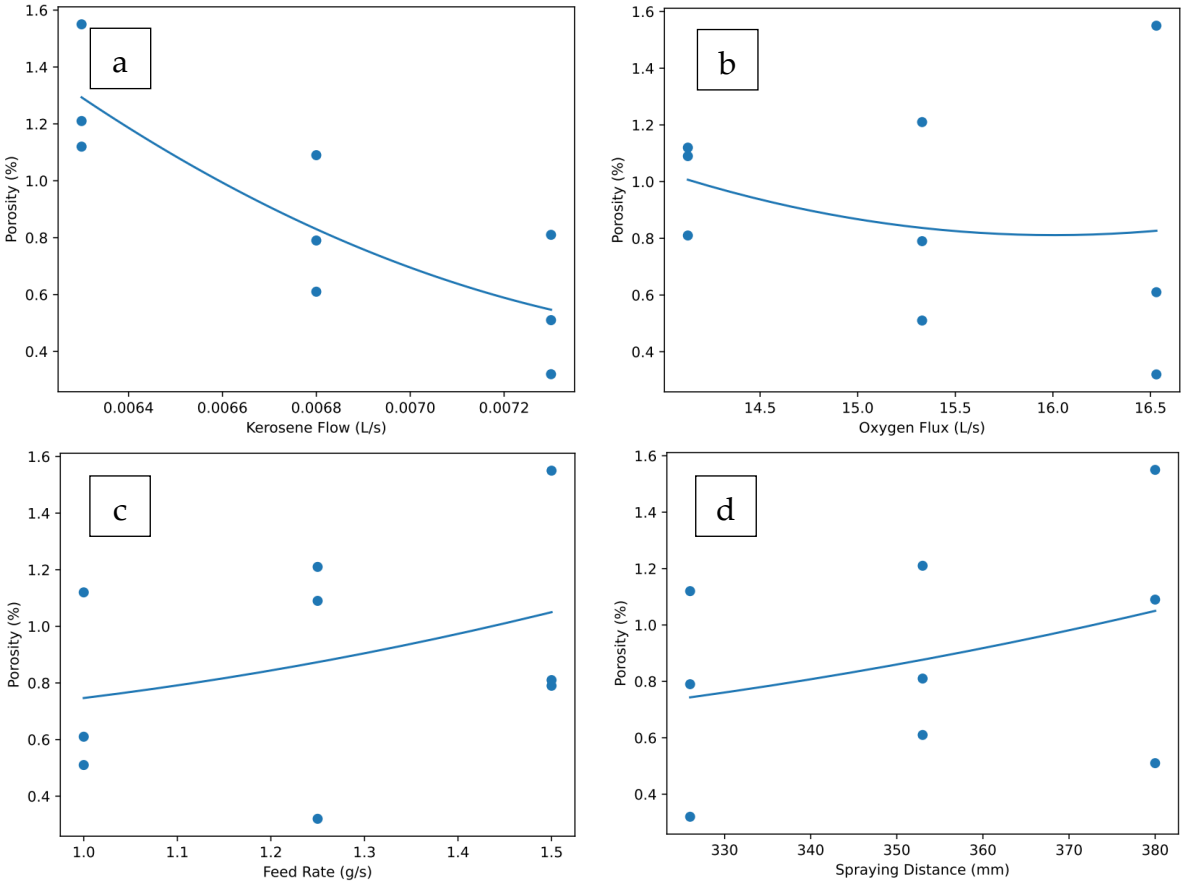


Figure 6. The regression graphs showing the relationship between the porosity of the WC-10Co-4Cr coating and the four factors of high-velocity oxygen-fuel (HVOF) spraying: (**a**) kerosene flow, (**b**) oxygen flow, (**c**) feed rate, (**d**) spray distance.

3.4. Relationship Between Vickers Hardness, Porosity, Abrasive Wear Rate, and Wear Mechanism

The relationship between Vickers hardness, porosity, and wear rate for the nine WC-10Co-4Cr coatings obtained from the orthogonal experiment is shown in Figure 7.

Figure 7 shows that the trend of coating porosity is generally consistent with the trend of wear rate and inversely correlated with coating hardness [21]. Based on the phase composition (Figure 3) and high-magnification microstructure (Figure 4c), the WC-10Co-4Cr coating consists primarily of hard WC particles embedded in a metallic binder phase (CoCr). The reduced hardness of WC-10Co-4Cr coatings with higher porosity can be attributed to their decreased load-bearing capacity and greater local deformation under indentation. This inverse relationship is reflected in the wear performance: the hardest coating (9#) had a wear rate of 0.569 $mm^3/(N{\cdot}m)$, representing an 80.6% reduction compared to the softest coating (3#) at 0.914 $mm^3/(N{\cdot}m)$. Notably, the wear resistance of both coatings was substantially higher than that of the AISI 1020 steel substrate (69.987 $mm^3/(N{\cdot}m)$). To further clarify the individual effects of kerosene flux (A), oxygen flux (B), powder feed rate (C), and spraying distance (D) on the coating wear rate, a second-order polynomial

regression was fitted using the L9 orthogonal experimental data. The regression equations were established as follows (3):

$$\text{Wear volume loss rate} = -1.69294 + 71.558A - 0.07384B - 1.003C + 0.007629D + 1.113 \times 105A^2 + 0.0513B^2 + 1.0373C^2 - 4.001 \times 10^{-5}D^2 \quad (3)$$

The fitted polynomial surface indicates that (i) increasing kerosene flux and oxygen flux tends to reduce wear rate within the tested range, (ii) excessively high powder feed rate or spraying distance leads to an increase in wear rate, and (iii) moderate parameter combinations favor minimizing the wear volume loss. These trends are consistent with typical HVOF processing mechanisms, where optimal energy input and particle melting conditions promote dense microstructures and improved wear resistance.

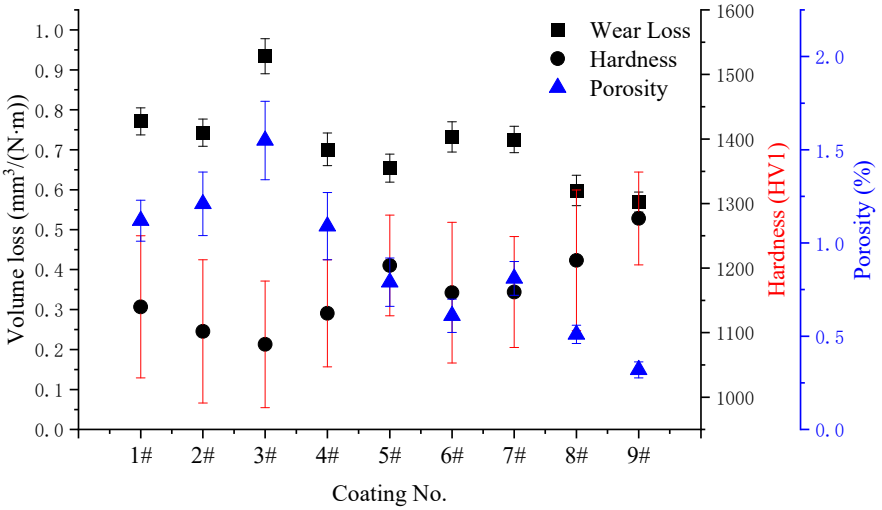


Figure 7. Vickers hardness, porosity, and wear rate of the WC-10Co-4Cr coatings.

The worn surface morphology of the WC-10Co-4Cr coating (9#) after abrasive wear testing is shown in Figure 8.

Figure 8 shows scratches and shallow grooves aligned with the abrasive direction on the surface of the binder phase, caused by the cutting action of SiO_2 abrasive particles. The presence of water in the slurry, as employed in this wet sand rubber wheel test, plays a critical role in modifying the abrasive wear mechanism. The aqueous medium can promote the rolling of abrasive particles and reduce the effective friction coefficient between the rubber wheel and the coating surface [22]. This altered contact condition tends to diminish the direct penetration (cutting) of abrasives and enhance their rolling and micro-ploughing actions. Consequently, under such wet conditions, the formation of shallow grooves and micro-ploughing on the binder phase becomes more predominant compared to deep cutting, which is more characteristic of dry abrasive wear.

In contrast, the WC particle surfaces show no obvious scratches, attributable to their higher hardness compared to SiO_2. Although the hard WC particles are not easily cut directly, they are susceptible to cracking under repeated scratching and impact from the abrasives due to their brittleness (marked I in Figure 8). Furthermore, when the surrounding binder phase is gradually worn away by the abrasives (marked II in Figure 8), these cracked or unsupported WC particles easily loosen and pull out (marked III in Figure 8). Thus, the wear mechanism involves micro-cutting and ploughing [23,24] of the soft binder phase by the abrasive particles, leading to the eventual loss of the hard WC particles due to lack of support [25]. The presence of water may further facilitate the removal of debris from the wear zone, potentially accelerating the pull-out of WC particles once they are loosened [26].

For coatings with lower hardness, the abrasive particles can more easily penetrate the surface. Additionally, in coatings with higher porosity, the bonding between WC particles and the binder is weaker, reducing the support for the carbides and accelerating material removal, resulting in higher wear rates for high-porosity/low-hardness coatings [3,9].

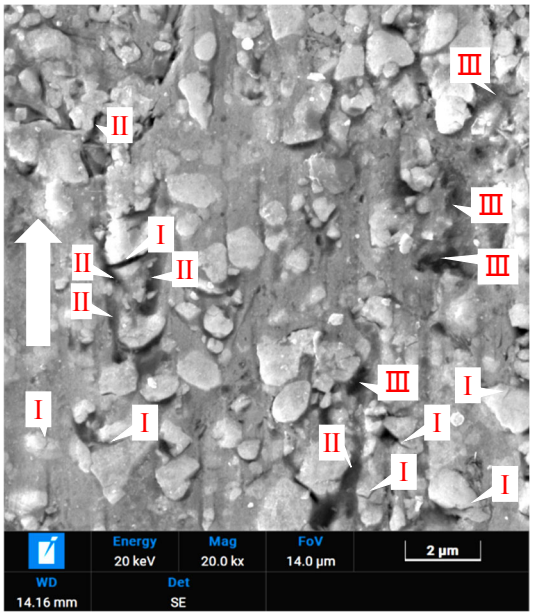


Figure 8. Microscopic morphology of the worn surface of 9# coating after abrasive wear (the white arrows indicate the movement direction of the abrasive particles during the wear process. I—cracked WC particle; II—region where the CoCr metallic binder phase is gradually worn away; III—pit left after the pull-out of a WC particle).

3.5. Electrochemical Corrosion Behavior and Mechanism

Numerous studies report that the corrosion resistance of WC-based coatings increases with their density [8–12]. Therefore, the coating with the highest density (9#) was selected for electrochemical testing, and its corrosion resistance was compared with the AISI 1020 steel substrate, as shown in Figure 9 and Table 2.

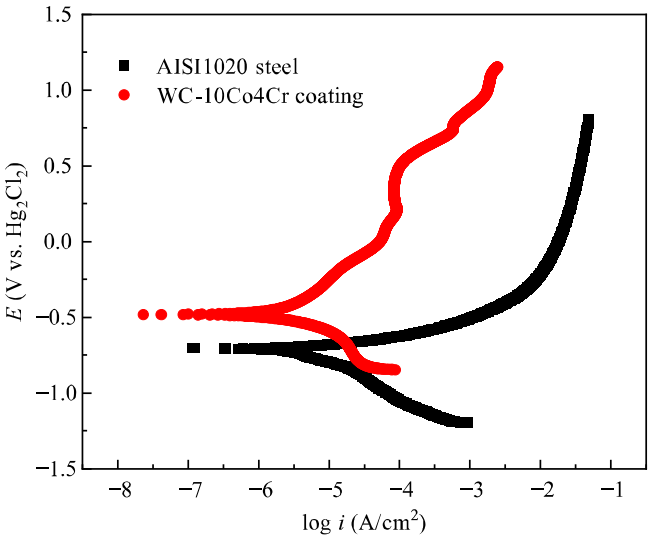


Figure 9. Electrochemical corrosion polarization curves of the WC-10Co-4Cr coating (9#) and AISI 1020 steel substrate.

Table 2. Open circuit potential and corrosion current density of the 9# WC-10Co-4Cr coating and AISI 1020 steel.

Specimen	OCP (V)	E_{corr} (V)	I_{corr} (A/cm^2)
AISI 1020 steel	−0.70	−0.71	6.37×10^{-6}
WC-10Co-4Cr coating	−0.35	−0.48	2.46×10^{-6}

Figure 9 and Table 2 indicate that the AISI 1020 steel substrate exhibits significantly lower open-circuit and corrosion potentials than the WC-10Co-4Cr coating, along with a notably higher corrosion current density. Moreover, the optimal WC-10Co-4Cr coating developed in this study demonstrates superior corrosion resistance compared to most HVOF-prepared WC-10Co-4Cr coatings reported in the literature [8–12]. The higher potential and lower corrosion current density observed in our coating reflect a reduced tendency for corrosion and thus better corrosion resistance. This improvement can be largely attributed to the coating's dense and uniform microstructure, which not only effectively hinders the penetration of liquid corrosive media but also promotes the formation of a more uniform protective film on the surface [27].

The surface microstructure of the WC-10Co-4Cr coating after electrochemical corrosion testing is shown in Figure 10.

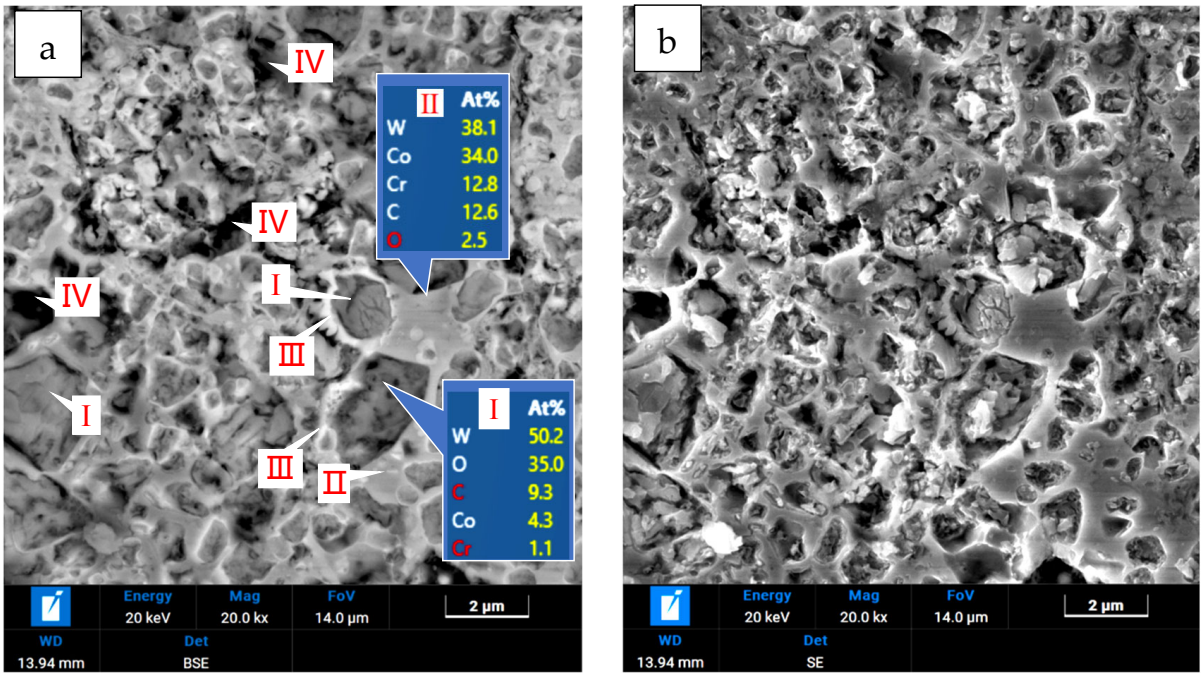


Figure 10. Surface microstructure of the WC-10Co-4Cr coating after electrochemical corrosion, (**a**) back scattered electron image, (**b**) secondary electron image (I—shallow pit with corrosion products, II—flat surface region, III—bright white ring around the pit, IV—deep pit).

(1) Pit areas containing corrosion products (marked I, high in W and O): the electrochemical corrosion of HVOF-sprayed WC-10Co-4Cr coatings in NaCl solution is a multi-stage process. It begins with micro-galvanic coupling between WC particles and the CoCr binder phase. The more active CoCr binder acts as the anode, undergoing preferential dissolution ($Co \rightarrow Co^{2+} + 2e^-$), accelerated by chloride ions (Cl^-). This leads to initial pit formation and weakens the support for WC particles. The exposed WC surface acts as the cathode, facilitating the oxygen reduction reaction ($O_2 + 2H_2O + 4e^- \rightarrow 4OH^-$), creating a locally alkaline microenvironment within the

confined pit. This alkalinity destabilizes WC, leading to its oxidative decomposition into soluble tungstate ions (e.g., $2WC + 4O_2 + 2H_2O \rightarrow 2WO_4^{2-} + 2CO + 4H^+$), which may subsequently re-deposit as W-rich oxides (e.g., WO_3) accumulating inside the pits (Region I) [1].

(2) Relatively flat regions (marked II): These regions contain Co and Cr along with W. The morphology suggests these are Co (Cr) solid solutions. The high Cr content imparts good corrosion resistance, explaining their relatively intact appearance after corrosion.

(3) Bright white annular rings at pit edges (marked III): These bright phases are W_2C and W formed from decarburization of WC particles during spraying. These phases remain after the surrounding material corrodes.

(4) Deeper pores/holes (marked IV): These may form after the loss of both WC particles and corrosion products, or they may originate from pre-existing large pores in the coating where accelerated pitting corrosion occurred due to trapped electrolyte.

In summary, the significant potential difference (100–300 mV) between WC (Ecorr ~ −0.1 V to +0.2 V vs. SCE) and Co (Ecorr ~ −0.4 V to −0.2 V vs. SCE) establishes a micro-galvanic cell in the electrolyte: Co (anode) dissolves ($Co \rightarrow Co^{2+} + 2e^-$), while WC (cathode) promotes oxygen reduction ($O_2 + 2H_2O + 4e^- \rightarrow 4OH^-$). Chloride ions destroy the passive film on Co and form complexes, accelerating Co dissolution [28].

Consequently, the failure of the WC-10Co-4Cr coating in NaCl solution is a typical electrochemical corrosion process originating from the electrochemical difference between the WC phase and the Co-based binder. The process involves preferential attack and dissolution of the Co-based binder phase, particularly areas with lower Cr content, by corrosive chloride ions [26]. This leads to the loss of support for the hard WC particles, causing them to detach [24], resulting in a roughened coating surface (Figure 10b).

4. Conclusions

In this study, WC-10Co-4Cr coatings were fabricated using HVOF thermal spraying. The effects of key process parameters on the microstructure, mechanical properties, abrasive wear resistance, and corrosion behavior were systematically investigated. The main findings are summarized as follows:

(1) The phase composition of the WC-10Co-4Cr coatings prepared under various parameters remained largely consistent with the initial spray powder, with WC as the predominant phase. The presence of only minor amounts of W_2C and trace W phases indicates effective suppression of decarburization and oxidation during the kerosene-fueled HVOF process, demonstrating high phase stability.

(2) Optimization via a four-factor, three-level orthogonal experiment identified the optimal HVOF spray parameters as: kerosene flow rate of 0.0073 L/s, oxygen flow rate of 15.33 L/s, powder feed rate of 1 g/s, and spraying distance of 326 mm. The coating deposited under this optimized condition exhibited a dense microstructure characterized by the highest microhardness of 1281 HV1 and the lowest porosity of 0.32%.

(3) A strong correlation was established between coating hardness, porosity, and wear performance. The microhardness was negatively correlated with both the wear rate and porosity. The dominant wear mechanism involved micro-cutting and ploughing of the binder phase by abrasives, leading to the subsequent loosening and pull-out of WC particles due to insufficient support.

(4) The corrosion mechanism in a 3.5 wt.% NaCl solution was primarily governed by the electrochemical potential difference between the WC particles and the CoCr binder phase, leading to the formation of micro-galvanic cells. This resulted in the preferential anodic dissolution of the CoCr binder. Chloride ions (Cl^-) further accelerated this

process by destroying the passive film, ultimately causing destabilization and loss of WC particles and the formation of corrosion pits and surface roughness.

(5) Compared to the AISI 1020 steel substrate, the optimized HVOF-sprayed WC-10Co-4Cr coating demonstrated a remarkable 122-fold improvement in abrasive wear resistance, coupled with superior corrosion resistance, underscoring its significant potential as a protective coating for components operating in synergistic corrosive-wear environments.

Author Contributions: Conceptualization, Q.W. and T.L.; methodology, Q.W. and Y.H.; software, Q.W. and J.L. (Jiajun Li); validation, Q.W., T.L., J.L. (Jianwu Liu) and H.L.; formal analysis, Q.W. and J.L. (Jiajun Li); investigation, T.L.; resources, H.L.; data curation, Q.W. and T.L.; writing—original draft preparation, T.L. and C.S.R.; writing—review and editing, C.S.R., Q.W. and J.L. (Jiajun Li); visualization, J.L. (Jianwu Liu); supervision, Q.W.; project administration, Q.W.; funding acquisition, Q.W. All authors have read and agreed to the published version of the manuscript.

Funding: This work was financially supported by the Natural Science Foundation of Hunan Province, China (2023JJ30153).

Data Availability Statement: Available upon enquiry. The data are not publicly available due to privacy concerns.

Conflicts of Interest: Author Tao Liu was employed by the company Petroleum Engineering and Technology Institute of Southwest Oil and Gas Branch, Sinopec. Authors Haifeng Li and Jianwu Liu were employed by the company Transmission R&D Center, AECC Hunan Aviation Powerplant Research Institute. The remaining authors declare that the research was conducted in the absence of any commercial or financial relationships that could be construed as a potential conflict of interest.

References

1. Kumar, R.; Bhandari, D.; Goyal, K. Slurry erosion behaviour of HVOF-sprayed coatings on hydro turbine steel: A review. *IOP Conf. Ser. Mater. Sci. Eng.* **2021**, *1033*, 012064. [CrossRef]
2. Bolelli, G.; Berger, L.M.; Börner, T.; Koivuluoto, H.; Lusvarghi, L.; Lyphout, C.; Vuoristo, P. Tribology of HVOF-and HVAF-sprayed WC-10Co4Cr hardmetal coatings: A comparative assessment. *Surf. Coat. Technol.* **2015**, *265*, 125–144. [CrossRef]
3. Zhou, S.; Zhou, H.; Zhou, G.; Zhou, Y.; Zhou, X. Sliding wear and solid-particle erosion resistance of WC-based coatings deposited by high-velocity oxy-fuel spraying. *Surf. Coat. Technol.* **2021**, *407*, 126759. [CrossRef]
4. Wood, R.J.K. Tribology of thermal sprayed WC-Co coatings. *Int. J. Refract. Met. Hard Mater.* **2010**, *28*, 82–94. [CrossRef]
5. Ding, X.; Wang, Q.; Tian, Y.; Yang, C.; Yuan, C.; Ramachandran, C.S. Microstructure and wear performance of CeO_2-modified micro-nano structured WC-CoCr coatings sprayed with HVOF. *Lubricants* **2023**, *11*, 188. [CrossRef]
6. Sarkar, S.; Bandyopadhyay, P.P. Role of carbide grit size and in-flight particle parameters on the microstructure, phases, and nanoscale properties of HVOF-sprayed WC-12Co coatings. *Surf. Coat. Technol.* **2024**, *484*, 130879. [CrossRef]
7. Sudaprasert, T.; Shipway, P.H.; McCartney, D.G. Sliding wear behaviour of HVOF-sprayed WC-Co coatings deposited with both gas-fueled and liquid-fueled systems. *Wear* **2003**, *255*, 943–949. [CrossRef]
8. Zhou, Y.K.; Liu, X.B.; Kang, J.J.; Yue, W.; Qin, W.B.; Ma, G.Z.; Wang, C.B. Corrosion behavior of HVOF-sprayed WC-10Co-4Cr coatings in the simulated seawater drilling fluid under the high pressure. *Eng. Fail. Anal.* **2020**, *109*, 104338. [CrossRef]
9. Wang, Q.; Zhang, S.; Cheng, Y.; Xiang, J.; Zhao, X.; Yang, G. Wear and corrosion performance of WC-10Co4Cr coatings deposited by different HVOF and HVAF spraying processes. *Surf. Coat. Technol.* **2013**, *218*, 127–136. [CrossRef]
10. Wang, Q.; Luo, S.; Wang, S.; Wang, H.; Ramachandran, C.S. Wear, erosion and corrosion resistance of HVOF-sprayed WC and Cr_3C_2 based coatings for electrolytic hard chrome replacement. *Int. J. Refract. Met. Hard Mater.* **2019**, *81*, 242–252. [CrossRef]
11. Wang, Q.; Zhong, Y.; Li, H. Effect of Cobalt and Chromium Content on Microstructure and Properties of WC-Co-Cr Coatings Prepared by High-Velocity Oxy-Fuel Spraying. *Materials* **2023**, *16*, 7003. [CrossRef]
12. Xing, Z.; Wang, N.; Fan, L.; Shang, L.; Yu, L. Investigation of the corrosion performance of HVOF-sprayed WC-CoCr coatings applied on offshore hydraulic equipment. *Rev. Adv. Mater. Sci.* **2025**, *64*, 20240066. [CrossRef]
13. Singh, S.P.; Verma, P.K.; Singh, S.; Kapoor, M.; Balu, R. Microstructural characterization and electrochemical behaviour of HVOF sprayed WC-Co-Cr coatings on 316L boiler steel. *Results Surf. Interfaces* **2024**, *16*, 100248. [CrossRef]
14. Fu, X.; Chen, X.; Deng, Y. Process optimization and performance study of WC-10Co-4Cr coatings prepared by HVOF-sprayed. *Int. J. Refract. Met. Hard Mater.* **2025**, *134*, 107420. [CrossRef]

15. *ASTM C633-13*; Standard Test Method for Adhesion or Cohesion Strength of Thermal Spray Coatings. ASTM International: West Conshohocken, PA, USA, 2013.
16. *ASTM G105-20*; Standard Test Method for Conducting Wet Sand/Rubber Wheel Abrasion Test. ASTM International: West Conshohocken, PA, USA, 2020.
17. *ASTM G59-97*; Standard Test Method for Conducting Potentiodynamic Polarization Resistance Measurements. ASTM International: West Conshohocken, PA, USA, 2023.
18. *ASTM G102-89*; Standard Practice for Calculation of Corrosion Rates and Related Information from Electrochemical Measurements. ASTM International: West Conshohocken, PA, USA, 2023.
19. Qadir, D.; Sharif, R.; Nasir, R.; Awad, A.; Mannan, H.A. A review on coatings through thermal spraying. *Chem. Pap.* **2024**, *78*, 71–91. [CrossRef]
20. Bortolotti, L.; Ruggiero, G.; Bolelli, G.; Lusvarghi, L.; Morelli, S.; Björklund, S.; Joshi, S. Effect of powder morphology on tribological performance of HVAF-sprayed WC-CoCr coatings. *Surf. Coat. Technol.* **2025**, *505*, 132090. [CrossRef]
21. Cao, Y.; Yin, Z.; Zhan, Y.; Wang, S.; Wen, D.; Wang, G.; Hou, D. Optimisation and wear performance analysis of laser-cladded WC-Fe-based coating. *Insight-Non-Destr. Test. Cond. Monit.* **2024**, *66*, 153–158. [CrossRef]
22. Qiao, L.; Wu, Y.; Hong, S.; Long, W.; Cheng, J. Wet abrasive wear behavior of WC-based cermet coatings prepared by HVOF spraying. *Ceram. Int.* **2021**, *47*, 1829–1836. [CrossRef]
23. Wang, Q.; Tang, Z.; Cha, L. Cavitation and sand slurry erosion resistances of WC-10Co-4Cr coatings. *J. Mater. Eng. Perform.* **2015**, *24*, 2435–2443. [CrossRef]
24. Wang, Q.; Chen, Z.; Ding, Z.X.; Chen, D. Abrasive wear behavior of WC reinforced Ni-based composite coating sprayed and fused by oxy-acetylene flame. *Surf. Rev. Lett.* **2009**, *16*, 475–485. [CrossRef]
25. Steinlechner, R.; de Oro Calderon, R.; Koch, T.; Linhardt, P.; Schubert, W.D. A study on WC-Ni cemented carbides: Constitution, alloy compositions and properties, including corrosion behaviour. *Int. J. Refract. Met. Hard Mater.* **2022**, *103*, 105750. [CrossRef]
26. Gee, M.G.; Gant, A.; Roebuck, B. Wear mechanisms in abrasion and erosion of WC/Co and related hardmetals. *Wear* **2007**, *263*, 137–148. [CrossRef]
27. Singh, N.; Mehta, A.; Vasudev, H.; Samra, P.S. A review on the design and analysis for the application of Wear and corrosion resistance coatings. *Int. J. Interact. Des. Manuf.* **2024**, *18*, 5381–5405. [CrossRef]
28. Zhang, Y.; Li, H.; Cui, L.; Yang, W.; Ma, G.; Chen, R.; Wang, A. Comparative study on tribocorrosion behavior of hydrogenated/hydrogen-free amorphous carbon coated WC-based cermet in 3.5 wt% NaCl solution. *Corros. Sci.* **2024**, *227*, 111738. [CrossRef]

Disclaimer/Publisher's Note: The statements, opinions and data contained in all publications are solely those of the individual author(s) and contributor(s) and not of MDPI and/or the editor(s). MDPI and/or the editor(s) disclaim responsibility for any injury to people or property resulting from any ideas, methods, instructions or products referred to in the content.